INTERNATIONAL JOURNAL OF HYDROGEN ENERGY 47 (2022) 37840–37849

Available online at www.sciencedirect.com

ScienceDirect

journal homepage: www.elsevier.com/locate/he

Oxygen-vacancy-rich Ru-clusters decorated Co/Ce oxides modifying ZIF-67 nanocubes as a high-efficient catalyst for $NaBH_4$ hydrolysis

Luyan Shi [a], *Ke Zhu* [a], *Yuting Yang* [a], *Yi Liu* [a], *Shoulei Xu* [c,***], *Tayirjan Taylor Isimjan* [b,**], *Xiulin Yang* [a,*]

[a] *Guangxi Key Laboratory of Low Carbon Energy Materials, School of Chemistry and Pharmaceutical Sciences, Guangxi Normal University, Guilin 541004, China*

[b] *Saudi Arabia Basic Industries Corporation (SABIC) at King Abdullah University of Science and Technology (KAUST), Thuwal 23955-6900, Saudi Arabia*

[c] *School of Physical Science and Technology, Guangxi University, 100 East Daxue Road, Nanning 530004, China*

HIGHLIGHTS

- Ru/Co_6Ce_1@ZIF-67 nanocubes are fabricated by surfactant-mediated and reduction methods.
- The catalyst shows a high HGR and TOF (413.9 min^{-1}) surpassing most recently reported catalysts.
- The catalyst exhibits a stable multi-cycle reusability for $NaBH_4$ hydrolysis.
- Oxygen vacancies and the synergy between different components are the keys to improve catalytic activity.

GRAPHICAL ABSTRACT

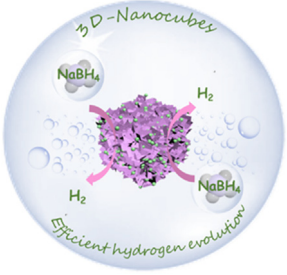

ARTICLE INFO

Article history:
Received 13 July 2022
Received in revised form
26 August 2022
Accepted 29 August 2022
Available online 17 September 2022

Keywords:
Ru/Co_6Ce_1@ZIF-67 catalyst
Oxygen vacancies

ABSTRACT

Designing a cost-effective and high-performance catalyst for $NaBH_4$ hydrolysis is a significant step in developing a sustainable hydrogen source. Herein, we prepared a cost-effective Ru-clusters decorated cobalt-cerium oxides coating ZIF-67 (Ru/Co_6Ce_1@ZIF-67) catalyst via a facile reduction method, displaying high performance and exceptional reusability in alkaline $NaBH_4$ solution. The optimized catalyst exhibits a high hydrogen generation rate (HGR, 5726.1 mL min^{-1} g^{-1}), turnover frequency (TOF, 413.9 mol_{H2} min^{-1} mol_{Ru}^{-1}), and low activation energy (E_a, 53.0 kJ mol^{-1}), surpassing most of the recently reported catalysts. Furthermore, the catalytic performance does not change considerably after five cycles, indicating the catalyst's multi-cycle reusability. Studies imply the uniquely

* *Corresponding author.*
** *Corresponding author.*
*** *Corresponding author.*
E-mail addresses: xsl@gxu.edu.cn (S. Xu), isimjant@sabic.com (T.T. Isimjan), xlyang@gxnu.edu.cn (X. Yang).

https://doi.org/10.1016/j.ijhydene.2022.08.289

$NaBH_4$ hydrolysis
Hydrogen generation

synergistic effect of Ru, Co/Ce oxides, abundant oxygen vacancies, as well as the porous nanocube structure, enabling the catalysts to possess high metal dispersion, outstanding catalytic performance and exceptional reusability. This work will open light on using an oxygen vacancies-rich strategy to design a high-activity catalyst for promoting $NaBH_4$ hydrolysis.

Introduction

Energy shortage and environmental pollution are the main factors affecting the quality of life [1]. There is a desperate need to mine green, renewable and efficient energy materials [2,3]. Hydrogen is an ideal alternative to traditional fuels due to its high energy density and zero CO_2 emission [4,5]. However, finding a cheap hydrogen storage method is often very challenging. $NaBH_4$ is a promising candidate among the various storage materials because of its high theoretical hydrogen content of 10.6 wt%, long-term stability in alkaline condition and nontoxicity [6,7]. $NaBH_4$ can also generate H_2 through hydrolysis under mild conditions, and the by-products are nontoxic [8]. Moreover, a recent study indicated that the $NaBH_4$ could be regenerated through by-product rehydrogenation, making it possible for the $NaBH_4$–H_2-PEMFC system to be a primary source for on-demand power supply [9]. Nevertheless, the self-hydrolysis of $NaBH_4$ releases H_2 slowly, and the overall conversion is only 7–8% at ambient temperature [10,11]. Consequently, designing efficient catalysts to promote sodium borohydride hydrolysis remains a critical issue.

Previous studies suggested that noble metal-based catalysts, such as Ru–Co-PEDOT [12] and Ru–Fe/Go [13], showed excellent catalytic activity and robust stability toward $NaBH_4$ hydrolysis [14]. However, the high cost, the lack of reserves, and the self-agglomeration limit industrial application [15,16]. Therefore, considerable afford has been dedicated to developing non-noble transition metals. Recently, cobalt-based catalysts are widely studied for hydrolysis of sodium borohydride due to the fact that its performance is particularly validated as the most effective non-noble metal among Ni-, Fe-, and Cu-based catalysts [17]. Among cobalt-based catalysts, cobalt oxides have been confirmed to be efficient catalyst [18]. Wei et al. [19] reported that Co_3O_4 hollow fiber catalyst exhibited good performance. However, the activity and stability of cobalt oxides catalysts were still lower than those of noble metal catalysts [20]. Many noble metal and cobalt oxide composite catalysts have been developed to achieve high performance while reducing costs. For example, Dou et al. [21] reported a high-efficiency Ru-clusters decorated CoO_x@NPC catalyst for hydrogen generation.

To address the aggregation of the metal nanoparticles during synthesis, suitable supports or organic capping agents should be introduced. Metal-organic frameworks (MOFs) are considered ideal support materials due to their unique properties, including exceptional porosity, structural diversity, large specific surface area, and chemical stability [22,23]. ZIF-67 is one of MOFs with imidazole as an organic linker with metal cobalt, which has a large specific surface area to prevent metal particles agglomeration and has proven to be highly stable in solution, even in alkaline solution at high temperatures [24,25]. Many studies have also shown that ZIF-67-supported composites catalysts exhibit remarkable performance in $NaBH_4$ hydrolysis for hydrogen production, e.g., Pd/PD-ZIF-67 [15], Ru/ZIF-67 [26] and so on. Given these merits, ZIF-67 appears to be an excellent substrate to promote $NaBH_4$ hydrolysis. Nonetheless, MOFs as carriers have low electrical conductivity, hindering the charge transfer during hydrolysis [27]. It can enhance electron transport by introducing oxygen vacancies created by rare earth elements, such as cerium oxide [28]. In cerium oxides, Ce^{3+} and Ce^{4+} coexist, and the electronic structure of Co species can be modified due to the existence of electronically flexible transitions and abundant oxygen vacancies between Ce^{3+} and Ce^{4+}, thereby enhancing the conductivity of Co-MOF and improving the performance of the catalyst [29,30]. Based on the above consideration, we assume that Ru cluster-modified Co oxides and doped Ce oxides have the potential to be an efficient catalyst for hydrolysis of sodium borohydride.

Here, we propose a facile surfactant-mediated and chemical reduction method to synthesize Ru/Co_6Ce_1@ZIF-67 catalyst with abundant oxygen vacancies for $NaBH_4$ hydrolysis in alkaline environments. The Ru clusters (~ 2.7 nm) decorated Co_6Ce_1@ZIF-67 nanocubes showed outstanding catalytic activity and remarkable reusability for $NaBH_4$ hydrolysis. It has a high HGR value of 5726.1 mL min^{-1} g^{-1} and a TOF value of 413.9 mol_{H2} min^{-1} mol_{Ru}^{-1}. Systematic investigations further demonstrate that the ZIF-67 support prevents Ru clusters aggregation, and oxygen vacancies can accelerate electronic transfer, promoting the reversible dissociation of B–H on active sites of Co oxides and Ru clusters, and finally stimulating hydrolysis of sodium borohydride. Furthermore, we proposed a plausible reaction mechanism according to the Michaelis-Menten model reported in the previous literature [31].

Experimental section

Materials

Cobalt nitrate hexahydrate ($Co(NO_3)_2 \cdot 6H_2O$, 99.0%, Aladdin), cerium nitrate hexahydrate ($Ce(NO_3)_3 \cdot 6H_2O$, 99.95%, Macklin), ruthenium (III) trichloride ($RuCl_3 \cdot xH_2O$, 99%, Ru:37–40%, Innochem), 2-methylimidazole (2-MI, 98%, Aladdin), cetyltrimethylammonium bromide (CTAB, 99.0%, Aladdin), sodium borohydride ($NaBH_4 \geq$ 98.0%, Sinopharm Group), sodium hydroxide (NaOH ≥96.0%, Xilong Science), ethanol (99.7%, Kelongchem). All chemicals were purchased from commercial

companies and could be used directly without further purification.

Synthesis of ZIF-67 nanocubes

Co-based zeolitic imidazolate framework (ZIF-67) nanocubes were prepared according to previous work with slightly modification [32]. In a typical procedure, 580 mg of $Co(NO_3)_2 \cdot 6H_2O$ was dissolved in 20 mL of deionized water containing 10 mg of CTAB. Then, this solution was rapidly injected into 140 mL of an aqueous solution containing 908 mg of 2-methylimidazole and stirred at room temperature for 20 min. The purple product was collected by centrifugation, washed three times with ethanol and vacuum-dried at 70 °C for 12 h.

Synthesis of Co_6Ce_1@ZIF-67

A total of 60 mg of ZIF-67 nanocubes was dispersed in 40 mL of ethanol to form solution A. 160 mg of $Co(NO_3)_2 \cdot 6H_2O$ and 40 mg of $Ce(NO_3)_3 \cdot 6H_2O$ were dissolved in 10 mL of ethanol to form solution B. Then, solution B was dripped on solution A under magnetic stirring and sonicated for 40 min to form a uniform solution. Finally, the product was collected by centrifugation, washed with ethanol three times, and vacuum-dried at 70 °C for 12 h. For comparison, under keeping the total mass of the metal salt at 0.2 g, other CoCe@ZIF-67 composites were prepared by altering the Co/Ce molar ration (1:1, 4:1, 6:1, 9:1, 12:1) during the synthesis process. The Co@ZIF-67 and Ce@ZIF-67 were prepared via the same routine without adding $Ce(NO_3)_3 \cdot 6H_2O$ or $Co(NO_3)_2 \cdot 6H_2O$.

Synthesis of Ru/Co_6Ce_1@ZIF-67

The Co_6Ce_1@ZIF-67 (80 mg) was added into a 50 mL glass beaker with 20 mL of deionized water and 15 mg of $RuCl_3 \cdot xH_2O$. After continuous stirring for 4 h, 10 mL of 2.6 M $NaBH_4$ solution (including 2 wt% NaOH) was added dropwise into the above mixture. After stirring for another 0.5 h, the resultant product crystal was separated by centrifugation, followed by multiple times washing in deionized water and ethanol, and subsequently dried in a vacuum at 70 °C for 12 h. Inductive coupled plasma atomic emission spectroscopy (ICP-AES) accurately determined the content of Ru species (Table S1) and the sample with 6.3 wt% showed the highest catalytic performance. Samples with Ru loadings of 4.5 wt% to 10.6 wt% were prepared by the same method, using $RuCl_3 \cdot xH_2O$ with different mass. As a comparison, a mass ratio of 6.3 wt% Ru was applied to synthesize all other contrastive catalysts. The Ru/Co@ZIF-67 and Ru/Ce@ZIF-67 were prepared using the same procedure mentioned above without $Ce(NO_3)_3 \cdot 6H_2O$ or $Co(NO_3)_2 \cdot 6H_2O$. In addition, Ru@ZIF-67 was synthesized by directly adding $RuCl_3 \cdot xH_2O$ into ZIF-67 solution, followed by a similar reduction treatment.

Synthesis of single Ru

200 mg of $RuCl_3 \cdot xH_2O$ was dissolved in 40 mL of deionized water via ultrasonication. After continuous stirring for 30 min, 10 mL of $NaBH_4$ solution was added into the above mixture. Finally, the black mixture was centrifuged to collect the sediment, which was washed at least three times with deionized water and ethanol, then dried under vacuum.

Catalytic hydrolysis of $NaBH_4$ measurements

The evolved hydrogen from the hydrolysis of $NaBH_4$ was collected and measured with a drainage method. A mixed solution of 25 mL, containing 150 mL $NaBH_4$ and 0.4 wt% NaOH, was injected to a three-necked round-bottom flask (100 mL), placed into a temperature-controlled water bath oscillator to keep it at 25 °C during the hydrolysis reaction. After 0.5 h, the prepared catalysts (10 mg) were dispersed in the above solution, rapidly plugging the flask. The instantaneous water volume changes were monitored by an electronic balance connected to a computer. Hydrolysis of $NaBH_4$ was also carried out at different temperatures (298–318 K) to obtain the activation energy. For the reusability study, the catalyst was recollected, washed with deionized water and ethanol, and dried in a vacuum at 70 °C after each cycle. The collected catalyst from the previous test was transferred to each process's new test solution. It was worth noting that the amount of motivation was the same as in the first cycle experiment. All tests were repeated three times to ensure reliable results.

Results and discussion

Synthetic method and crystallinity analysis

The design strategy of the Ru/Co_6Ce_1@ZIF-67 is illustrated in Fig. 1a. Firstly, ZIF-67 nanocubes are prepared through a surfactant-mediated method. Afterward, the as-prepared ZIF-67 nanocubes were mixed with $Co(NO_3)_2 \cdot 6H_2O$ and $Ce(NO_3)_3 \cdot 6H_2O$ to form Co–Ce oxides on the surface of ZIF-67 nanocubes. Finally, the Ru species are introduced into the Co_6Ce_1@ZIF-67 by an ambient temperature reduction for producing the Ru/Co_6Ce_1@ZIF-67. The crystallinity of as-prepared catalysts is first analyzed by X-ray diffraction (XRD). As shown in Fig. 1b, pure ZIF-67 nanocubes and Ru/Co_6Ce_1@ZIF-67 share the same XRD patterns, while the intensity of the peaks varies between them. However, there is no apparent diffraction peak of the cobalt-cerium oxides, implying the low-loading and/or amorphous nature of the composite. Such amorphous characteristics are beneficial for catalytic materials with higher performance than crystalline material because they can supply larger ion-accessible surface area and sufficient redox-active centers [33]. Furthermore, no characteristic peaks of Ru clusters are observed in the XRD pattern of Ru/Co_6Ce_1@ZIF-67 due to the low Ru loading, which the fuzzy lattice fringes can confirm in the TEM images of Ru/Co_6Ce_1@ZIF-67 [34]. As shown in Fig. 1c, we resort to the electron paramagnetic resonance (EPR) spectra for direct oxygen vacancies identification. The apparent symmetrical signals at $g = 2.003$ correspond to oxygen vacancies of the samples [35]. An increase in the oxygen vacancy signal intensity is observed after introducing the Ce component in Ru/Co@ZIF-67, which can massively alter the electronic properties of the composite, thereby enhancing the catalytic activity [36].

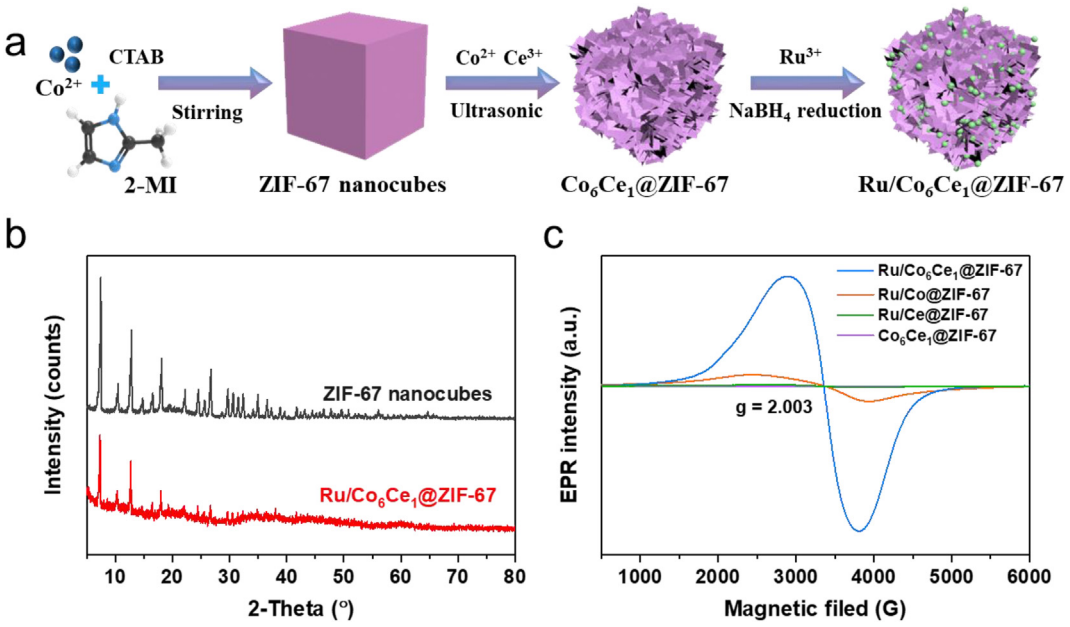

Fig. 1 – (a) Schematic diagram of the synthesis of Ru/Co_6Ce_1@ZIF-67. (b) XRD patterns of ZIF-67 nanocubes and Ru/Co_6Ce_1@ZIF-67. (c) EPR spectra of the synthesized Ru/Co_6Ce_1@ZIF-67, Ru/Co@ZIF-67, Ru/Ce@ZIF-67 and Co_6Ce_1@ZIF-67.

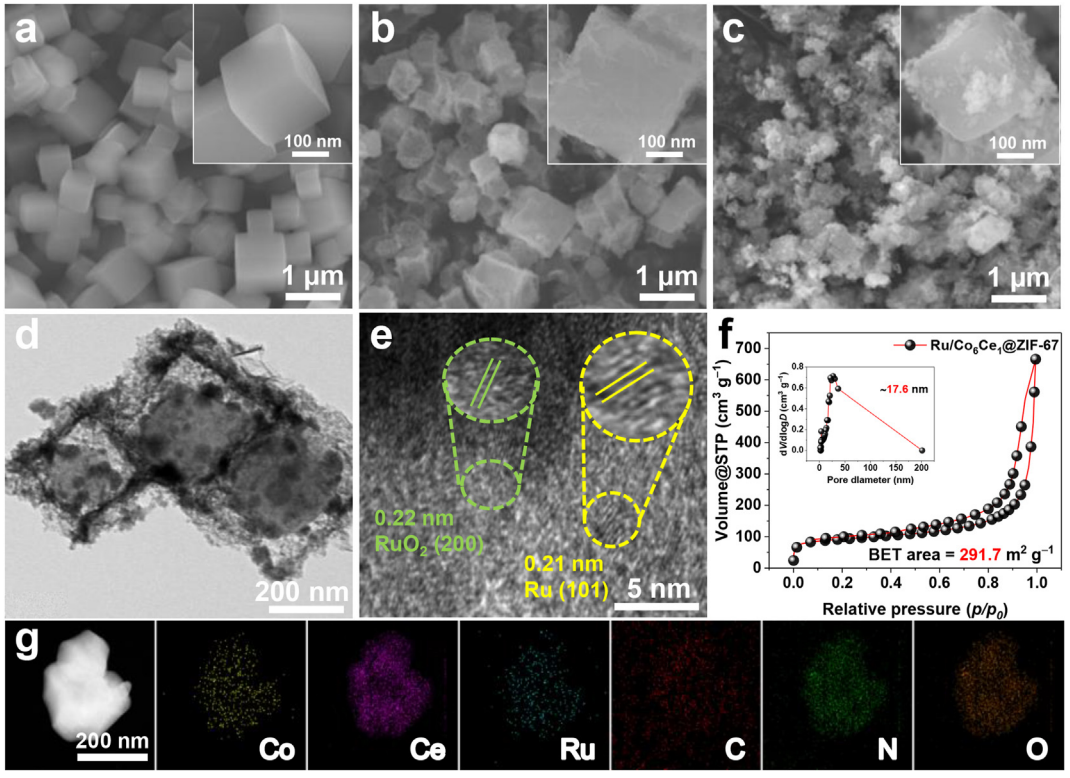

Fig. 2 – Scanning electron microscopy (SEM) of (a) ZIF-67 nanocubes, (b) Co_6Ce_1@ZIF-67 and (c) Ru/Co_6Ce_1@ZIF-67 (Insets are high-magnification SEM images). (d) Transmission electron microscopy (TEM) and (e) high-resolution TEM images of Ru/Co_6Ce_1@ZIF-67. (f) N_2 adsorption/desorption isotherms with pore-size distribution curve (inset) of Ru/Co_6Ce_1@ZIF-67. (g) HAADF-STEM image of Ru/Co_6Ce_1@ZIF-67 and corresponding elemental mappings of Co, Ce, Ru, C, N, and O.

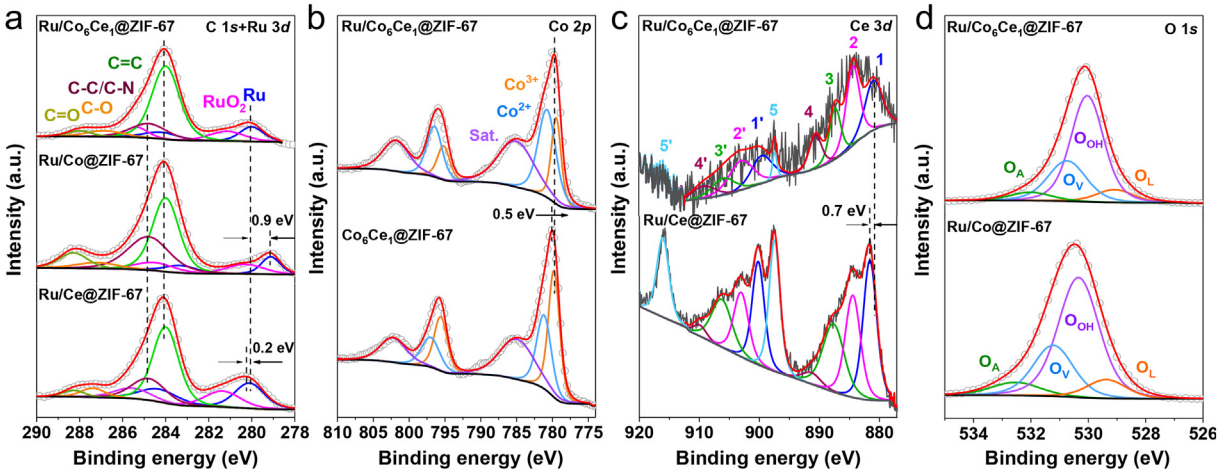

Fig. 3 – High-resolution XPS spectra of (a) C 1*s* + Ru 3*d*, (b) Co 2*p*, (c) Ce 3*d* and (d) O 1*s* regions of Ru/Co_6Ce_1@ZIF-67, Ru/Co@ZIF-67, Ru/Ce@ZIF-67 and Co_6Ce_1@ZIF-67, respectively.

Microstructure analysis

The morphological features and microstructure of the catalysts are analyzed by scanning electron microscopy (SEM) and transmission electron microscopy (TEM). Fig. 2a shows the as-formed ZIF-67 nanocube morphology with a smooth surface. The further reaction with excess $Co(NO_3)_2 \cdot 6H_2O$ and $Ce(NO_3)_3 \cdot 6H_2O$ under sonication for 40 min leads to formation of Co_6Ce_1@ZIF-67 nanocubes. Fig. 2b reveals that the SEM image of Co_6Ce_1@ZIF-67 nanocubes still maintains the cubic shape. But the surface of the products become rough, and the higher magnification image displays that the Co_6Ce_1 oxides appear to be a nanosheet. After introducing Ru, the sample has cubic characteristics with some distended nanoparticles on the surface, loosely stacked together (Fig. 2c). These results suggest that introducing a specific number of Co/Ce oxides and Ru clusters does not destroy the cube-like framework of the ZIF-67-based derivative. As show in Fig. 2d, the TEM image shows that Ru/Co_6Ce_1@ZIF-67 exhibits a yolk-shell structure consisting of solid ZIF-67 yolk and Ru/Co_6Ce_1 shell, similar to the literature reports [37,38]. Each nanocube is uniformly decorated with dark Ru clusters with a size of ~2.7 nm (Fig. S1). According to the high-resolution TEM image of Ru/Co_6Ce_1@-ZIF-67, Fig. 2e shows that the lattice spacing of 0.21 nm are indexed to Ru (101) crystal plane [39]. The interplanar spacing of 0.22 nm are attributed to the (200) crystal plane of RuO_2 [40]. The N_2 adsorption–desorption isotherms of Ru/Co_6Ce_1@ZIF-67 displays the type IV isotherm with a remarkable hysteresis loop, indicating the existence of mesopores [41]. The Brunauer-Emmett-Teller (BET) specific surface area and pore size are 291.7 $m^2\ g^{-1}$ and ~17.6 nm (Fig. 2f). These results show that the multiporous 3D frame structure and high surface area of Ru/Co_6Ce_1@ZIF-67 benefit ions' fast diffusion and expose more active sites, which can enhance the catalytic activity [42,43]. In addition, the EDX spectrum (Fig. S2) manifests the presence of Ru, Co, Ce, C, N, and O, and elemental mapping images elucidate that all the elements are homogenously distributed throughout the Ru/Co_6Ce_1@ZIF-67 catalyst (Fig. 2g).

X-ray photoelectron spectroscopy analysis

X-ray photoelectron spectroscopy (XPS) has been further conducted to investigate the relationship between the charge and chemical valence states on the surface of the catalysts. As shown in Fig. S3, the XPS survey spectra of Ru/Co_6Ce_1@ZIF-67 verify the presence of C, N, O, Co, Ce and Ru elements, agreeing well with the above HAADF-STEM elemental mapping and EDX results. The high-resolution C 1*s* + Ru 3*d* spectrum (Fig. 3a) are deconvoluted into C=C (284.0 eV), C–C (284.8 eV) and used as a calibration standard [44]. The two peaks at 280.0 and 284.2 eV binding energies attribute to metallic Ru^0 [21], whereas the peaks at 281.2 eV and 285.4 eV correspond to RuO_2. This surface oxide could be formed from exposure of the samples to atmosphere during the reaction. Compared to the Ru/Co@ZIF-67, the binding energy of Ru is positively shifted by 0.9 eV, indicating that the Ce doping can effectively tune the electronic structure of Ru/Co_6Ce_1@ZIF-67, thereby regulating efficient charge transfer [45]. Compared with the Ru/Ce@ZIF-67 sample, the binding energy of Ru is negatively shifted by 0.2 eV, which indicates that there is a strong charge-transfer interaction between Ru clusters and Co oxides [46]. Fig. 3b displays the Co 2*p* high-resolution spectrum, where the binding energies of 779.5, 780.8 and 785.3 eV can be coincided with Co^{3+}, Co^{2+}, and the satellite peak [47]. The binding energies of Co on Ru/Co_6Ce_1@ZIF-67 exhibit a negative shift compared to the Co_6Ce_1@ZIF-67, which confirms that the introduction of Ru clusters has a great influence on the electronic states of the surrounding Co atoms. Typically, the Co^{2+}/Co^{3+} ratio of the Ru/Co_6Ce_1@ZIF-67 is higher than that of Co_6Ce_1@ZIF-67, suggesting that the part of Co^{3+} is reduced to Co^{2+} after introducing Ru to create oxygen vacancies [48]. Interestingly, it has been reported that oxygen vacancies can accelerate electronic transfer and increase the conductivity of the catalyst, laying the foundation for improving catalytic performance [49,50].

The Ce 3*d* spectrum of Ru/Co_6Ce_1@ZIF-67 is fitted with five pairs of spin-energy separations (Fig. 3c). The characteristic peaks located at 880.9 eV, 887.3 eV (1, 3) and 899.5 eV, 905.9 eV

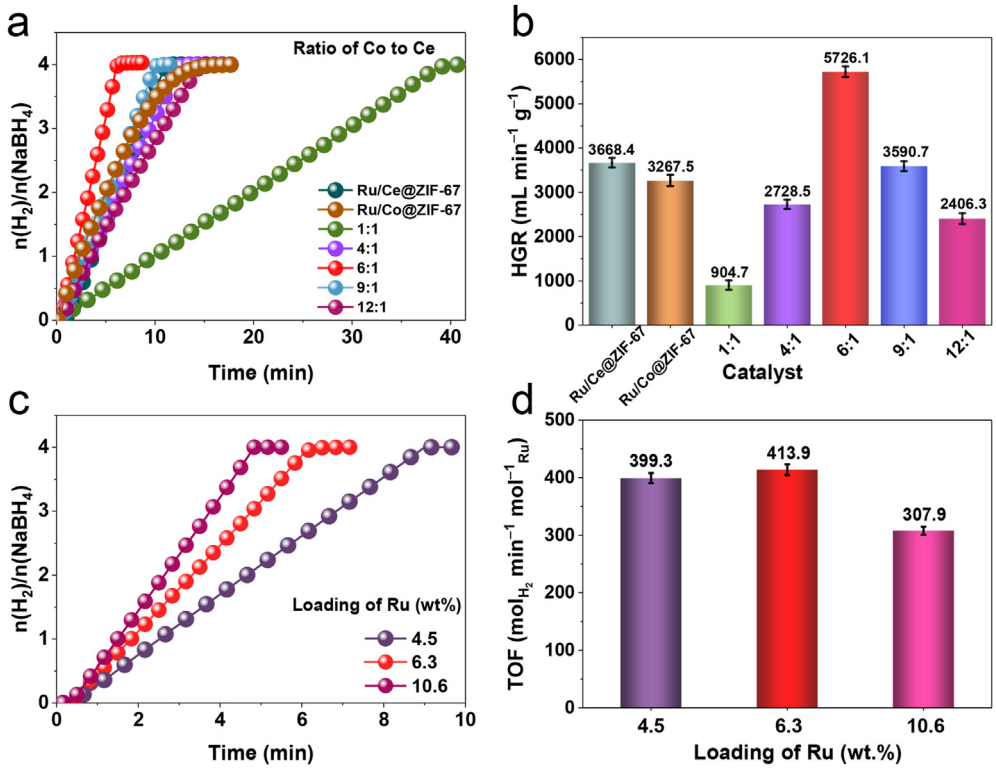

Fig. 4 – (a) Curves of hydrolysis of alkaline $NaBH_4$ solution with different rations of Co/Ce, and (b) the corresponding H_2 evolution rate values. (c) Curves of hydrolysis of alkaline $NaBH_4$ solution with different loadings of Ru species on Ru/Co_6Ce_1@ZIF-67 catalysts, and (d) the summarized TOF values.

(1′, 3′) are assigned to Ce^{3+} ($3d^{10}4f^1$ initial electronic state), whereas the six peaks at 884.4 eV, 890.6eV, 897.4eV (2, 4, 5) and 903.0 eV, 909.2 eV, 916.0 eV (2′, 4′, 5′) are attributed to Ce^{4+} ($3d^{10}4f^0$ initial electronic state) [51,52]. In the Ce 3*d* spectra, the Ce^{3+} co-exists with Ce^{4+} in the composite [53]. Clearly, the peak of Ce^{3+} in Ru/Co_6Ce_1@ZIF-67 shows a negative shift of about 0.7 eV compared to Ru/Ce@ZIF-67, implying the electrostatic interactions between Ce oxides and surrounding Co oxides. It is worth noting that the Ce^{3+} ions interact with surrounding atoms such as Co through lone electron existing in the $4f^1$ orbital. In addition, oxygen vacancies can be created on the catalyst surface due to the charge compensation of Ce^{3+} ions [54]. The above analyses prove that the introduction of Ce can generate more oxygen vacancies, thereby enhancing the catalyst's performance [55]. Furthermore, we detect the oxygen vacancies by O 1s XPS spectra. Fig. 3d shows that the O 1s spectra can be deconvoluted into four peaks. The peaks of ~529.1 eV, ~530.0 eV, ~530.7 eV and ~532.0 eV can be attributed to lattice oxygen (O_L), oxygen atoms bound to hydroxyl species (O_{OH}), oxygen vacancy (O_v) and absorbed oxygen (O_A), respectively [56,57]. The integral area ratio of oxygen vacancy peaks in Ru/Co_6Ce_1@ZIF-67 (26.3%) is more significant than that in Ru/Co@ZIF-67 (24.6%), implying that oxygen vacancies increase after the introduction of Ce component, which is in line with the EPR results.

Catalytic hydrolysis analysis

The catalytic activities are assessed in alkaline $NaBH_4$ solution at 25 °C, and the volume of H_2 is measured by a water displacement method. The hydrolysis setup is schematically illustrated in Fig. S4. The $NaBH_4$ (150 mM) aqueous solution shows almost no self-hydrolysis (Fig. S5), and negligible hydrogen gas is produced from 150 mM $NaBH_4$ + 0.4 wt% NaOH solution indicating $NaBH_4$ is stable in both water and under an alkaline solution (Fig. S6). As shown in Fig. 4a and b, we investigate the effect of catalysts fabricated by different molar ratios of Co/Ce on H_2 generation. When the molar ratio of Co/Ce is 6:1, Ru/Co_6Ce_1@ZIF-67 exhibits the best activity and is superior to those of Ru/Co@ZIF-67 and Ru/Ce@ZIF-67. And the HGR value is superior to those currently reported literature (Table S2). Simultaneously, the optimal Ru loading has been researched in great detail. As displayed in Fig. 4c–d, a higher Ru loading shows a higher H_2 release rate, but the TOF values show a volcano-shape curve. When the content of Ru is 6.3 wt %, the corresponding TOF reaches a maximum value of 413.9 mol_{H2} min^{-1} mol_{Ru}^{-1}.

As shown in Fig. 5a and b, the Ru/Co_6Ce_1@ZIF-67 catalyst only takes about 6 min to achieve the complete hydrolysis of sodium borohydride. Notably, for Ru/ZIF-67 and Ru catalysts, sodium borohydride hydrolyzed only about 35% and 10% within 6 min, while Co_6Ce_1@ZIF-67 and ZIF-67 had almost no activity. These results showed that Ru/Co_6Ce_1@ZIF-67 exhibited the highest performance relative to all control catalysts, indicating that Ru is the predominate active site and Co_6Ce_1@ZIF-67 plays a crucial role in catalytic hydrolysis [58]. The analysis suggests that the synergistic effect of different components and abundant oxygen vacancies in the Ru/Co_6Ce_1@ZIF-67 hybrid catalyst are the main factors for the high catalytic performance. The influence of $NaBH_4$ concentration

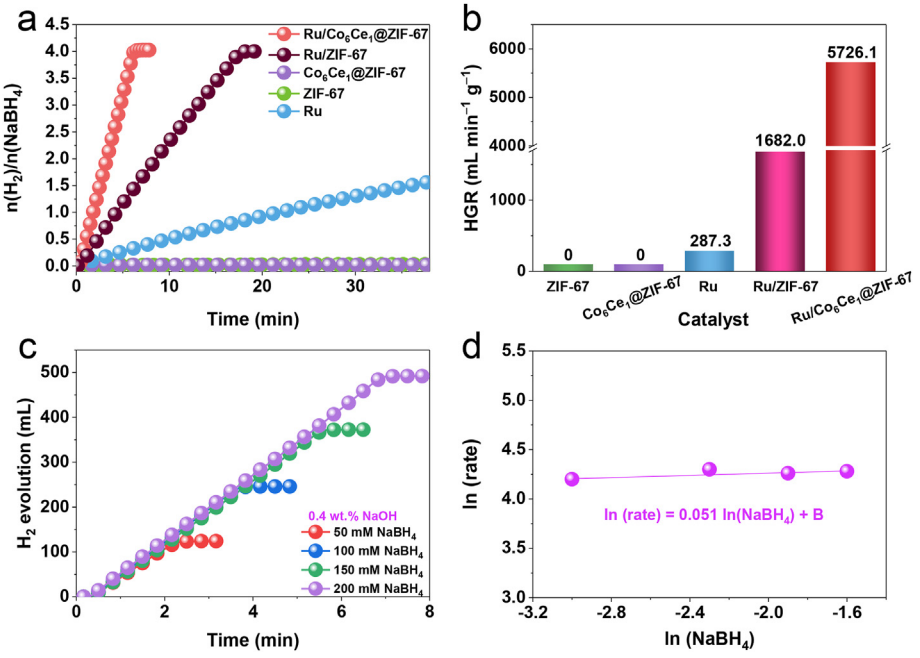

Fig. 5 – (a) Curves of hydrolysis of alkaline $NaBH_4$ solution with different kinds of catalysts, and (b) the corresponding H_2 evolution rate values. (c) The relationship between H_2 evolution and different $NaBH_4$ concentrations and (d) the corresponding plot of ln (rate) *vs* ln (concentration of $NaBH_4$).

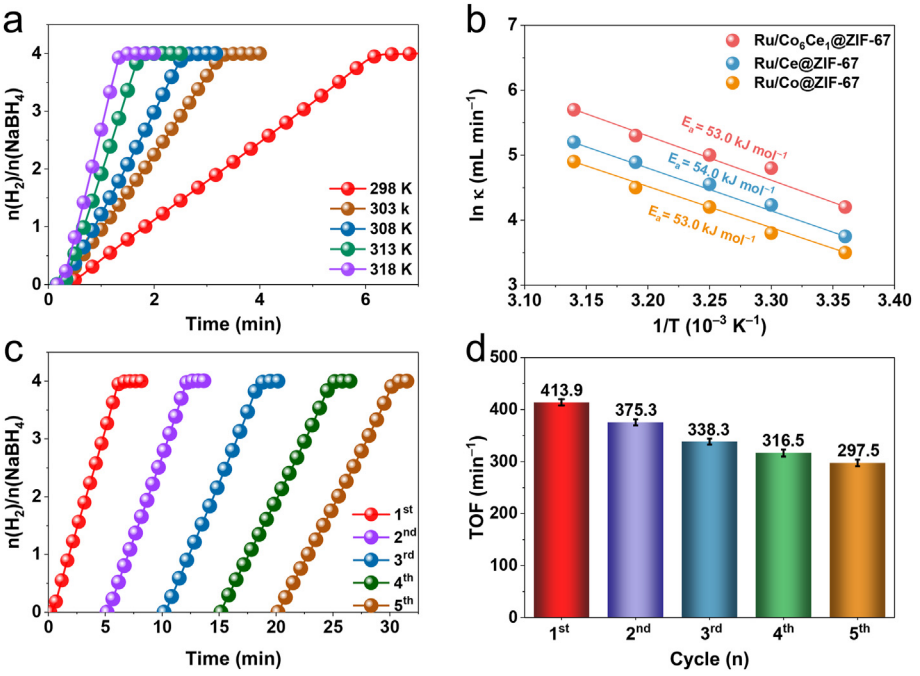

Fig. 6 – (a) Curves of hydrolysis of alkaline $NaBH_4$ solution with different reaction temperatures, and (b) the calculated activation energies of Ru/Co_6Ce_1@ZIF-67, Ru/Co@ZIF-67 and Ru/Ce@ZIF-67 catalysts. (c) Recycling stability test of Ru/Co_6Ce_1@ZIF-67 catalyst in alkaline $NaBH_4$ solution at 25 °C and (d) the corresponding TOF values in the different recycling test.

has also been explored at 25 °C with 10 mg Ru/Co_6Ce_1@ZIF-67. Fig. 5c reveals that the hydrogen generation rate does not change significantly. Meanwhile, the relation between ln (rate) and ln ($NaBH_4$) has been given in Fig. 5d, where the slope value is calculated to be 0.051, which is negligible and indicates a zero-order reaction kinetics [59]. NaOH is often used as a stabilizing agent to prevent the self-hydrolysis of $NaBH_4$. Fig. S7 shows the effect of NaOH concentration on hydrogen

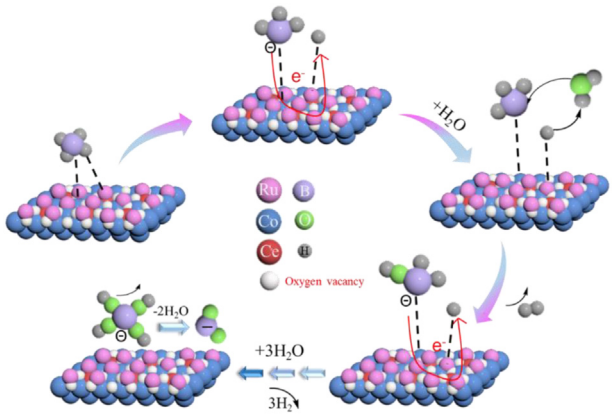

Fig. 7 – Proposed catalytic mechanism schematic of Ru/Co_6Ce_1@ZIF-67 catalyst for H_2 generation by hydrolysis of alkalized $NaBH_4$ solution.

generation from $NaBH_4$ hydrolysis, which indicates that the addition of NaOH can greatly promote the catalytic hydrolysis of $NaBH_4$. Notably, the H_2 generation rate remains almost unchanged when the NaOH concentration is increased from 0.4 wt% to 10 wt%. Therefore, we select 0.4 wt% as the optimal NaOH concentration in this work, which can avoid wasting the reagent.

The effect of temperature on hydrogen generation rate is studied in the range of 298 K–318 K (Fig. 6a and Fig. S8). The results show an increase in HGR with the increase in reaction temperature. According to the Arrhenius plot, the calculated E_a of Ru/Co_6Ce_1@ZIF-67 and Ru/Co@ZIF-67 are 53.0 kJ mol^{-1}, which are slightly lower than that of Ru/Ce@ZIF-67 (54.0 kJ mol^{-1}) (Fig. 6b). The reusability of Ru/Co_6Ce_1@ZIF-67 in $NaBH_4$ hydrolysis at 25 °C are probed using the same catalyst in 5 successive cycles. As displayed in Fig. 6c–d, H_2 yields over five cycles are almost the same (taking approximately 6.2, 7.2, 8.5, 9.8 and 10.5 min, respectively), and the TOF values decrease each time slightly. After five cycles, Ru/Co_6Ce_1@ZIF-67 catalyst still preserves its pristine morphology, except that some Ru clusters fall off from the surface (Fig. S9). As can be seen from Fig. S10, compared with the initial catalyst, the content ratio of Ru, Co^{2+}, Ce^{3+} is slightly increased, indicating the partial RuO_2, Co^{3+} and Ce^{4+} have been reduced in the process of hydrolysis. However, the XPS spectra of O 1s show that the oxygen vacancy concentration is reduced from 26.3% to 17.0%. Thus, the slight decrease in catalytic activity may be mainly attributed to Ru clusters exfoliation, decreased oxygen vacancy concentration and poisoning [60].

Catalytic mechanism analysis

Based on the above analysis, the proposed mechanism for the catalytic hydrolysis of $NaBH_4$ is shown in Fig. 7. From the above XPS study, it can be known that the binding energy of Ru clusters in Ru/Co_6Ce_1@ZIF-67 is negatively shifted compared to Ru/Ce@ZIF-67, suggesting electrons are transferred from Co oxides to Ru clusters. Consequently, the electron density of the Co oxides is greater than Ru clusters. Hence, BH_4^- takes place a reversible dissociation on active sites of Co oxides and Ru clusters, resulting in electron-deficient BH_3^- adsorbed on Co oxides sites, and H adsorbed on Ru clusters sites. The negative charge of BH_3^- is transferred to H through oxygen vacancies [61]. The adsorbed H reacts with an H from free water to release H_2. The BH_3 transfers its surplus hydride to the Ru clusters sites after the OH^- reacts with the adsorbed BH_3. Finally, the $BH_2(OH)^-$ is formed. The reaction continues following a resemblant route until the formation of $B(OH)_4^-$ and $4H_2$ [31].

Conclusion

In summary, a controllable and straightforward approach was developed to construct an oxygen-vacancy-rich Ru/Co_6Ce_1@ZIF-67 nanocube catalyst for $NaBH_4$ hydrolysis. MOF support favors the Ru clusters adsorption, decreasing Ru loading and preventing active species from migration and aggregation. The optimized Ru/Co_6Ce_1@ZIF-67 delivers impressively catalytic activity toward alkaline $NaBH_4$ solution by showing a higher HGR value and excellent reusability. Characteristic studies certify that the significance of synergistic effects among Ru, Co, and Ce enabled more active sites and oxygen vacancies. Interestingly, oxygen vacancies serve as a transport channel to accelerate electron mobility and enhance the catalyst's performance. In particular, the oxygen vacancy-enriched Ru/Co_6Ce_1@ZIF-67 catalyst constructed in this work can be easily synthesized at ambient temperature, which is helpful for large-scale production. The Ru/Co_6Ce_1@ZIF-67 catalyst for hydrolysis of sodium borohydride has an excellent industrial perspective due to its low cost, durability, and high performance. Meanwhile, the synthesis of low-cost Ru/Co_6Ce_1@ZIF-67 catalysts enables on-site hydrogen production, thereby reducing the cost of high-pressure hydrogen storage. Due to these unique advantages, the Ru/Co_6Ce_1@ZIF-67 catalyst is highly promising for a portable catalytic $NaBH_4$ hydrolysis system for hydrogen generation. Overall, we consider that the Ru/Co_6Ce_1@ZIF-67 catalyst for hydrolysis of sodium borohydride is a viable process on an industrial scale. This work also paves a new avenue for the practical application of sodium borohydride hydrolysis to hydrogen production.

Declaration of competing interest

The authors declare that they have no known competing financial interests or personal relationships that could have appeared to influence the work reported in this paper.

Acknowledgements

This work has been supported by the National Natural Science Foundation of China (no. 21965005), Natural Science Foundation of Guangxi Province (2018GXNSFAA294077, 2021GXNSFAA076001), Project of High-Level Talents of Guangxi (FKA18015), and Guangxi Technology Base and Talent Subject (GUIKEAD18126001, GUIKE 20297039 CE).

Appendix A. Supplementary data

Supplementary data to this article can be found online at https://doi.org/10.1016/j.ijhydene.2022.08.289.

REFERENCES

[1] Zhang Y, Long X, Liu X, Chen G, Zhang N, Li M, et al. Superlattice-like Co-doped Mn oxide and NiFe hydroxide nanosheets toward an energetic oxygen evolution reaction. ACS Sustainable Chem Eng 2022;10:5683–92.

[2] Shao X, Yang Y, Liu Y, Yan P, Zhou S, Taylor Isimjan T, et al. Oxygen vacancy-rich N-doped carbon encapsulated BiOCl-CNTs heterostructures as robust electrocatalyst synergistically promote oxygen reduction and Zn-air batteries. J Colloid Interface Sci 2022;607:826–35.

[3] Wang F, Zhang Y, Zhang J, Yuan W, Li Y, Mao J, et al. In situ electrochemically formed Ag/NiOOH/Ni_3S_2 heterostructure electrocatalysts with exceptional performance toward oxygen evolution reaction. ACS Sustainable Chem Eng 2022;10:5976–85.

[4] Peng Q, Shao X, Hu C, Luo Z, Taylor Isimjan T, Dou Z, et al. Co_4S_3 grafted 1 T-phase dominated WS_2 ultrathin nanosheet arrays for highly efficient overall water splitting in alkaline media. J Colloid Interface Sci 2022;615:577–86.

[5] He F, Han Y, Tong Y, Zhong M, Wang Q, Su B, et al. NiFe alloys@N-doped graphene-like carbon anchored on N-doped graphitized carbon as a highly efficient bifunctional electrocatalyst for oxygen and hydrogen evolution reactions. ACS Sustainable Chem Eng 2022;10:6094–105.

[6] Abdelhamid HN. A review on hydrogen generation from the hydrolysis of sodium borohydride. Int J Hydrogen Energy 2021;46:726–65.

[7] Ouyang L, Zhong H, Li H-W, Zhu M. A recycling hydrogen supply system of $NaBH_4$ based on a facile regeneration process: a review. INORGA 2018;6:10.

[8] Tuan DD, Huang C-W, Duan X, Lin C-H, Lin K-YA. Cobalt-based coordination polymer-derived hexagonal porous cobalt oxide nanoplate as an enhanced catalyst for hydrogen generation from hydrolysis of borohydride. Int J Hydrogen Energy 2020;45:31952–62.

[9] Nunes HX, Silva DL, Rangel CM, Pinto AMFR. Rehydrogenation of sodium borates to close the $NaBH_4$-H_2 cycle: a review. Energies 2021;14:3567.

[10] Kojima Y, Kawai Y, Nakanishi H, Matsumoto S. Compressed hydrogen generation using chemical hydride. J Power Sources 2004;135:36–41.

[11] Boran A, Erkan S, Ozkar S, Eroglu I. Kinetics of hydrogen generation from hydrolysis of sodium borohydride on Pt/C catalyst in a flow reactor. Int J Energy Res 2013;37:443–8.

[12] Chowdhury AD, Agnihotri N, De A. Hydrolysis of sodium borohydride using Ru–Co-PEDOT nanocomposites as catalyst. Chem Eng J 2015;264:531–7.

[13] Zhang Y, Zou J, Luo Y, Wang F. Study on preparation and performance of Ru-Fe/GO catalyst for sodium borohydride alcoholysis to produce hydrogen. Fullerenes, Nanotub Carbon Nanostruct 2020;28:786–93.

[14] Lu D, Yu G, Li Y, Chen M, Pan Y, Zhou L, et al. RuCo NPs supported on MIL-96(Al) as highly active catalysts for the hydrolysis of ammonia borane. J Alloys Compd 2017;694:662–71.

[15] Wu C, Guo J, Zhang J, Zhao Y, Tian J, Isimjan TT, et al. Palladium nanoclusters decorated partially decomposed porous ZIF-67 polyhedron with ultrahigh catalytic activity and stability on hydrogen generation. Renew Energy 2019;136:1064–70.

[16] Paladini M, Arzac GM, Godinho V, Hufschmidt D, de Haro MCJ, Beltrán AM, et al. The role of cobalt hydroxide in deactivation of thin film Co-based catalysts for sodium borohydride hydrolysis. Appl Catal B Environ 2017;210:342–51.

[17] Yao L, Li X, Peng W, Yao Q, Xia J, Lu Z-H. Co-CeO_x nanoparticles anchored on a nitrogen-doped carbon nanosheet: a synergistic effect for highly efficient hydrolysis of sodium borohydride. Inorg Chem Front 2021;8:1056–65.

[18] Liu H, Shi Q, Yang Y, Yu Y-N, Zhang Y, Zhang M, et al. CoO-Co_2P composite nanosheets as highly active catalysts for sodium borohydride hydrolysis to generate hydrogen. Funct Mater Lett 2020;13.

[19] Wei L, Dong X, Ma M, Lu Y, Wang D, Zhang S, et al. Co_3O_4 hollow fiber: an efficient catalyst precursor for hydrolysis of sodium borohydride to generate hydrogen. Int J Hydrogen Energy 2018;43:1529–33.

[20] Wu C, Zhang J, Guo J, Sun L, Ming J, Dong H, et al. Ceria-Induced strategy to tailor Pt atomic clusters on cobalt–nickel oxide and the synergetic effect for superior hydrogen generation. ACS Sustainable Chem Eng 2018;6:7451–7.

[21] Dou S, Zhang W, Yang Y, Zhou S, Rao X, Yan P, et al. Shaggy-like Ru-clusters decorated core-shell metal-organic framework-derived CoO_x@NPC as high-efficiency catalyst for $NaBH_4$ hydrolysis. Int J Hydrogen Energy 2021;46:7772–81.

[22] Tang T, Yuan R, Guo N, Zhu J, Gan X, Li Q, et al. Improving the surface area of metal organic framework-derived porous carbon through constructing inner support by compatible graphene quantum dots. J Colloid Interface Sci 2022;623:77–85.

[23] Quan Y, Shen R, Ma R, Zhang Z, Wang Q. Sustainable and efficient manufacturing of metal-organic framework-based polymer nanocomposites by reactive extrusion. ACS Sustainable Chem Eng 2022;10:7216–22.

[24] Park KS, Ni Z, Côté AP, Choi JY, Huang R, Uribe-Romo FJ, et al. Exceptional chemical and thermal stability of zeolitic imidazolate frameworks. Proc Natl Acad Sci U S A 2006;103:10186–91.

[25] Hanif S, Shi X, Iqbal N, Noor T, Anwar R, Kannan AM. ZIF derived PtNiCo/NC cathode catalyst for proton exchange membrane fuel cell. Appl Catal B Environ 2019;258:117947.

[26] Tuan DD, Lin K-YA. Ruthenium supported on ZIF-67 as an enhanced catalyst for hydrogen generation from hydrolysis of sodium borohydride. Chem Eng J 2018;351:48–55.

[27] Zhang Y, Xu J, Zhou J, Wang L. Metal-organic framework-derived multifunctional photocatalysts. Chin J Catal 2022;43:971–1000.

[28] Guo J, Wang B, Yang D, Wan Z, Yan P, Tian J, et al. Rugae-like Ni_2P-CoP nanoarrays as a bi-functional catalyst for hydrogen generation: $NaBH_4$ hydrolysis and water reduction. Appl Catal B Environ 2020;265:118584.

[29] Dong C, Zhou Y, Ta N, Liu W, Li M, Shen W. Shape impact of nanostructured ceria on the dispersion of Pd species. Chin J Catal 2021;42:2234–41.

[30] Sun Y, Guan Y, Wu X, Li W, Li Y, Sun L, et al. ZIF-derived "senbei"-like Co9S8/CeO2/Co heterostructural nitrogen-doped carbon nanosheets as bifunctional oxygen electrocatalysts for Zn-air batteries. Nanoscale 2021;13:3227–36.

[31] Demirci UB, Miele P. Reaction mechanisms of the hydrolysis of sodium borohydride: a discussion focusing on cobalt-based catalysts. C R Chim 2014;17:707–16.

[32] Dou S, Hu C, Shi L, Zhang W, Zhou S, Yan P, et al. Well-dispersed Ru-clusters decorating nanobox-structured CoP

synergistically catalyze the $NaBH_4$ hydrolysis and electro-reductive H_2 evolution. ChemCatChem 2021;13:3628–35.
[33] Wang Q, Gao F, Xu B, Cai F, Zhan F, Gao F, et al. ZIF-67 derived amorphous $CoNi_2S_4$ nanocages with nanosheet arrays on the shell for a high-performance asymmetric supercapacitor. Chem Eng J 2017;327:387–96.
[34] Gao T, Li X, Chen X, Zhou C, Yue Q, Yuan H, et al. Ultra-fast preparing carbon nanotube-supported trimetallic Ni, Ru, Fe heterostructures as robust bifunctional electrocatalysts for overall water splitting. Chem Eng J 2021;424:130416.
[35] Yang Y, Huang Y, Zhou S, Liu Y, Shi L, Isimjan TT, et al. Delicate surface vacancies engineering of Ru doped MOF-derived Ni-NiO@C hollow microsphere superstructure to achieve outstanding hydrogen oxidation performance. J Energy Chem 2022;72:395–404.
[36] Cao Y, Su Y, Xu L, Yang X, Han Z, Cao R, et al. Oxygen vacancy-rich amorphous FeNi hydroxide nanoclusters as an efficient electrocatalyst for water oxidation. J Energy Chem 2022;71:167–73.
[37] Lyu F, Bai Y, Li Z, Xu W, Wang Q, Mao J, et al. Self-templated fabrication of CoO–MoO_2 nanocages for enhanced oxygen evolution. Adv Funct Mater 2017;27:1702324.
[38] Lai J, Huang B, Chao Y, Chen X, Guo S. Strongly coupled nickel–cobalt nitrides/carbon hybrid nanocages with Pt-like activity for hydrogen evolution catalysis. Adv Mater 2019;31:1805541.
[39] Kwon IS, Debela TT, Kwak IH, Park YC, Seo J, Shim JY, et al. Ruthenium nanoparticles on cobalt-doped 1T′ phase MoS_2 nanosheets for overall water splitting. Small 2020;16:2000081.
[40] Liu J, Zheng Y, Jiao Y, Wang Z, Lu Z, Vasileff A, et al. NiO as a bifunctional promoter for RuO_2 toward superior overall water splitting. Small 2018;14:1704073.
[41] Gao Z, Fan G, Liu M, Yang L, Li F. Dandelion-like cobalt oxide microsphere-supported RuCo bimetallic catalyst for highly efficient hydrogenolysis of 5-hydroxymethylfurfural. Appl Catal B Environ 2018;237:649–59.
[42] Li D, Zhang Q, Shen Z, Siddharth K, Chen L, Shao M, et al. 3D hexapod-shaped Co-ZIFs-S derived co nanoparticles embedded into nitrogen and sulfur co-doped carbon decorated with ruthenium nanoparticles as efficient catalyst for rechargeable lithium oxygen battery. Nano Energy 2022;91:106644.
[43] Zhou S, Yang Y, Zhang W, Rao X, Yan P, Isimjan TT, et al. Structure-regulated Ru particles decorated P-vacancy-rich CoP as a highly active and durable catalyst for $NaBH_4$ hydrolysis. J Colloid Interface Sci 2021;591:221–8.
[44] Hu Y, Yu H, Qi L, Dong J, Yan P, Taylor Isimjan T, et al. Interface engineering of needle-like P-doped MoS_2/CoP arrays as highly active and durable bifunctional electrocatalyst for overall water splitting. ChemSusChem 2021;14:1565–73.
[45] Wang C, Shang H, Li J, Wang Y, Xu H, Wang C, et al. Ultralow Ru doping induced interface engineering in MOF derived ruthenium-cobalt oxide hollow nanobox for efficient water oxidation electrocatalysis. Chem Eng J 2021;420:129805.
[46] Li T, Zhang X, Chen Y, Zhong L, Li S, Zhang P, et al. Boosting the water dissociation kinetics via charge redistribution of ruthenium decorated on S, N-codoped carbon. J Mater Chem 2021;9:16967–73.
[47] Guo Y, Hong X, Wang Y, Li Q, Meng J, Dai R, et al. Multicomponent hierarchical Cu-doped NiCo-ldh/CuO double arrays for ultralong-life hybrid fiber supercapacitor. Adv Funct Mater 2019;29.
[48] Li Q, Huang F, Li S, Zhang H, Yu X-Y. Oxygen vacancy engineering synergistic with surface hydrophilicity modification of hollow Ru doped CoNi-ldh nanotube Arrays for boosting hydrogen evolution. Small 2022;18:2104323.
[49] Li Z, Zhang Y, Feng Y, Cheng C-Q, Qiu K-W, Dong C-K, et al. Co_3O_4 nanoparticles with ultrasmall size and abundant oxygen vacancies for boosting oxygen involved reactions. Adv Funct Mater 2019;29:1903444.
[50] Zhong H, Alberto Estudillo-Wong L, Gao Y, Feng Y, Alonso-Vante N. Oxygen vacancies engineering by coordinating oxygen-buffering CeO_2 with CoO_x nanorods as efficient bifunctional oxygen electrode electrocatalyst. J Energy Chem 2021;59:615–25.
[51] Yao Q, Lu Z-H, Yang Y, Chen Y, Chen X, Jiang H-L. Facile synthesis of graphene-supported Ni-CeO_x nanocomposites as highly efficient catalysts for hydrolytic dehydrogenation of ammonia borane. Nano Res 2018;11:4412–22.
[52] Bui HT, Weon S, Bae JW, Kim E-J, Kim B, Ahn Y-Y, et al. Oxygen vacancy engineering of cerium oxide for the selective photocatalytic oxidation of aromatic pollutants. J Hazard Mater 2021;404:123976.
[53] Chen X, Zhan S, Chen D, He C, Tian S, Xiong Y. Grey Fe-CeO_2-σ for boosting photocatalytic ozonation of refractory pollutants: roles of surface and bulk oxygen vacancies. Appl Catal B Environ 2021;286:119928.
[54] Sivanantham A, Ganesan P, Shanmugam S. A synergistic effect of Co and CeO_2 in nitrogen-doped carbon nanostructure for the enhanced oxygen electrode activity and stability. Appl Catal B Environ 2018;237:1148–59.
[55] Liu Z, Li B, Feng Y, Jia D, Li C, Sun Q, et al. Strong electron coupling of Ru and vacancy-rich carbon dots for synergistically enhanced hydrogen evolution reaction. Small 2021;17:2102496.
[56] Liu S, Zhang H, Hu E, Zhu T, Zhou C, Huang Y, et al. Boosting oxygen evolution activity of NiFe-LDH using oxygen vacancies and morphological engineering. J Mater Chem 2021;9:23697–702.
[57] Tang Y, Shen H, Cheng J, Liang Z, Qu C, Tabassum H, et al. Fabrication of oxygen-vacancy abundant NiMn-layered double hydroxides for ultrahigh capacity supercapacitors. Adv Funct Mater 2020;30:1908223.
[58] Yang Y, Dai Q, Shi L, Liu Y, Isimjan TT, Yang X. Electronic modulation of Pt nanoparticles on Ni_3N-Mo_2C by support-induced strategy for accelerating hydrogen oxidation and evolution. J Phys Chem Lett 2022;13:2107–16.
[59] Zhang H, Zhang L, Rodríguez-Pérez IA, Miao W, Chen K, Wang W, et al. Carbon nanospheres supported bimetallic Pt-Co as an efficient catalyst for $NaBH_4$ hydrolysis. Appl Surf Sci 2021;540:148296.
[60] Zhou L, Meng J, Li P, Tao Z, Mai L, Chen J. Ultrasmall cobalt nanoparticles supported on nitrogen-doped porous carbon nanowires for hydrogen evolution from ammonia borane. Mater Horiz 2017;4:268–73.
[61] Guo J, Wu C, Zhang J, Yan P, Tian J, Shen X, et al. Hierarchically structured rugae-like RuP_3–CoP arrays as robust catalysts synergistically promoting hydrogen generation. J Mater Chem 2019;7:8865–72.